Am J Cancer Res 2026;16(11):4756-4776
www.ajcr.us /ISSN:2156-6976/ajcr0176556

Original Article

LINC00294 interacts with CSTF1 to inhibit triple-negative breast cancer by reversing LCN2-associated ferroptosis resistance

Aijia Zhang, Xin Guo, Ya Wang, Ziqi Zhao, Fei Wang, Zhen Ning, Zhengang Cai, Guoyu Mu, Hongjiang Wang

First Affiliated Hospital of Dalian Medical University, Dalian 116000, Liaoning, China

Received September 8, 2026; Accepted October 15, 2026; Epub November 15, 2026; Published November 30, 2026

Abstract: Triple-negative breast cancer (TNBC) represents a highly malignant breast cancer subtype lacking effective targeted therapies. However, the biological function and underlying mechanisms of the long non-coding RNA (lncRNA) LINC00294 in TNBC remain unknown. This study aimed to elucidate its role and regulatory network in TNBC. LINC00294 expression was assessed in TNBC tissues and cell lines using RT-qPCR. CCK-8, Transwell, wound-healing, and flow-cytometry assays were performed to evaluate the effects of LINC00294 overexpression on TNBC cells. RNA pull-down coupled with mass spectrometry was employed to identify LINC00294-interacting proteins. mRNA-seq, RT-qPCR, Western blotting, and ferroptosis-related assays were conducted to elucidate the downstream molecular mechanisms. Finally, a xenograft tumor model was used to assess the in vivo phenotypic relevance of these findings. LINC00294 was significantly downregulated in TNBC tissues and cell lines. Overexpression of LINC00294 suppressed TNBC cell proliferation, migration, and invasion, and induced apoptosis. Mechanistically, LINC00294 interacted with cleavage stimulation factor subunit 1 (CSTF1), as identified by RNA pull-down coupled with mass spectrometry. CSTF1 overexpression counteracted the suppressive effects of LINC00294 on the malignant behavior of TNBC cells. mRNA-seq identified lipocalin-2 (LCN2) as a candidate downstream target of the LINC00294/CSTF1 axis. LCN2 overexpression decreased Fe^{2+} accumulation and lipid peroxidation and altered ferroptosis-related protein expression; these effects were reversed by CSTF1 knockdown or treatment with the ferroptosis inducer erastin. In xenograft tumor models, LINC00294 overexpression inhibited tumor growth, downregulated LCN2 expression, and promoted ferroptosis-associated changes, all of which were reversed by CSTF1 overexpression. These findings indicate that LINC00294 suppresses TNBC progression through its interaction with CSTF1, with LCN2 identified as a putative downstream mediator of ferroptosis resistance, highlighting the therapeutic potential of targeting this axis for TNBC.

Keywords: Triple-negative breast cancer, LINC00294, CSTF1, LCN2, ferroptosis

Introduction

Triple-negative breast cancer (TNBC) is an aggressive breast cancer subtype characterized by the absence of estrogen receptor (ER), progesterone receptor (PR), and human epidermal growth factor receptor 2 (HER2), which results in limited therapeutic options and poor patient prognosis [1-3]. Given the absence of canonical hormone receptors and HER2, which renders conventional targeted therapies inapplicable, attention is shifting toward the genomic "dark matter" of TNBC - thousands of non-protein-coding transcripts whose expression patterns closely mirror the disease's remarkable heterogeneity and aggressive clinical behavior [4-6].

Current research has identified various long non-coding RNAs (lncRNAs) that play critical roles in cancer biology [6, 7]. Many studies have suggested that lncRNAs can modulate key signaling pathways associated with cancer progression. For instance, BC069792 functions as a molecular sponge for hsa-miR-658 and hsa-miR-4739, thereby upregulating potassium voltage-gated channel Q4 protein expression, inhibiting JAK2 and p-AKT activities, and ultimately suppressing breast cancer growth [8]. Similarly, LINC01089 inhibits β-catenin expres-

https://doi.org/10.62347/OHDV3439

sion at the transcriptional level, thereby blocking the Wnt/β-catenin pathway and downstream target gene expression to suppress cell proliferation and invasion in breast cancer [9].

In recent years, the role of LINC00294 in cancer has attracted increasing attention. Studies have indicated that LINC00294 can serve as a prognostic biomarker for colorectal cancer patients [10, 11], and its overexpression inhibits proliferation, cell cycle progression, migration, and invasion in various tumor cells [10-12]. However, in cervical cancer, high LINC00294 expression upregulates cell cycle-related factors while downregulating the cell-cycle inhibitory factors p16 and p21, thereby exerting oncogenic effects [13]. Similarly, in hepatocellular carcinoma (HCC), LINC00294 is upregulated in tumor tissues and associated with tumor grade and patient prognosis. It stimulates HCC cell proliferation and the Warburg effect, thereby enhancing tumor progression [14]. The mechanisms underlying these context-dependent effects remain incompletely understood. Despite growing recognition of the importance of LINC00294 in cancer [11], the functional mechanisms of LINC00294 in TNBC remain largely unexplored.

The objective of this study was to elucidate the molecular mechanisms by which LINC00294 interacts with proteins (particularly RNA-binding proteins) and how these interactions influence the malignant phenotypes of TNBC cells. We employed RT-qPCR, CCK-8 assays, RNA pull-down, mRNA-seq, Transwell migration assays, siRNA-mediated knockdown, overexpression studies, flow cytometry, wound-healing assays, and animal models to systematically analyze LINC00294 expression levels and its functional regulatory effects in TNBC. Elucidation of these molecular mechanisms will not only enhance our understanding of TNBC biology but may also pave the way for innovative treatment strategies that could improve patient outcomes.

Materials and methods

Clinical samples

Eleven paired TNBC and adjacent normal tissues were collected at the First Affiliated Hospital of Dalian Medical University with written informed consent (Ethics No. PJ-KS-KY-2025-355). The inclusion criteria were as follows: (I) female patients histopathologically diagnosed with primary TNBC, defined as ER < 1%, PR < 1%, and HER2-negative (immunohistochemistry score 0/1+, or 2+ with negative fluorescence/chromogenic in situ hybridization) according to the ASCO/CAP guidelines; (II) no neoadjuvant chemotherapy, radiotherapy, or endocrine therapy before surgery; (III) availability of paired TNBC and adjacent normal tissues (≥ 2 cm from the tumor margin) resected en bloc during surgery; and (IV) complete clinicopathological data. The exclusion criteria were as follows: (I) a history of any other malignant tumor; (II) receipt of neoadjuvant or adjuvant anti-tumor therapy before tissue collection; (III) poor sample quality or insufficient tumor cellularity (< 50%) on hematoxylin-eosin review; and (IV) incomplete clinical records. The median age of the patients was 52 years (range: 38-65). Regarding tumor size, 3 cases (27.3%) were ≤ 2 cm, and 8 cases (72.7%) were > 2 cm. Histological grading revealed 5 cases (45.5%) as grade II and 6 cases (54.5%) as grade III. According to TNM staging, 7 cases (63.6%) were stage I-II, and 4 cases (36.4%) were stage III. Lymph node metastasis was present in 4 cases (36.4%) and absent in 7 cases (63.6%). The Ki-67 proliferation index was ≥ 20% in 9 cases (81.8%), indicating high proliferative activity.

Cell culture

The TNBC cell lines MDA-MB-231 and BT-549 and the non-tumorigenic breast epithelial cell line MCF-10A were purchased from Jiangsu KeyGEN Biotechnology Co., Ltd. (KeyGEN BioTECH, Nanjing, China). MDA-MB-231 cells were cultured in Leibovitz's L-15 medium supplemented with 10% fetal bovine serum (FBS) and 1% penicillin/streptomycin (P/S) in a humidified incubator at 37°C in a CO_2-free atmosphere. BT-549 cells were maintained in RPMI-1640 medium with 10% FBS, 10 μg/mL Insulin, and 1% P/S at 37°C in a humidified atmosphere of 5% CO_2. All cell lines were authenticated by short tandem repeat (STR) profiling and routinely tested negative for mycoplasma. MCF-10A cells were grown in a proprietary complete medium (KGL7001-500, KeyGEN BioTECH) at 37°C in a humidified atmosphere of 5% CO_2.

Construction of stable cell lines overexpressing LINC00294

Full-length LINC00294 was cloned into the pLVX-IRES-Puro vector. Lentiviruses were packaged in 293T cells and used to infect TNBC cells at an appropriate multiplicity of infection. Stable lines were selected with puromycin. LINC00294-overexpressing stable cell lines and negative control cell lines were constructed by KeyGEN BioTECH.

Cell transfection and treatment

The coding sequences of cleavage stimulation factor subunit 1 (CSTF1) and lipocalin 2 (LCN2) were cloned into the pcDNA3.1 vector to generate the CSTF1 overexpression plasmid (oe-CSTF1) and the LCN2 overexpression plasmid (oe-LCN2), respectively. Cells were transfected with oe-CSTF1, oe-LCN2, CSTF1 siRNA (si-CSTF1), or negative control (NC) using KeyGEN MAX 3000 transfection reagent (KeyGEN BioTECH) according to the manufacturer's instructions. For ferroptosis rescue experiments, cells were pretreated with 10 μM erastin for 2 h, followed by transfection and continued incubation for 48 h. All plasmids and siRNAs were constructed or synthesized by KeyGEN BioTECH. The CSTF1 siRNA sequences are listed in Table S1.

CCK-8 assay

After 48 h of treatment, cells were reseeded at a density of 1×10^4 cells/well in 96-well plates. Cell viability was assessed using CCK-8 (KeyGEN BioTECH) after an additional 24 h. The absorbance at 450 nm was measured using a Spark microplate reader (Tecan, Switzerland). For the CCK-8 assay, cells were reseeded 48 h after treatment, and viability was measured after an additional 24 h to capture the proliferative capacity of an equal number of seeded cells, whereas the Transwell and wound-healing assays required an additional 24-h incubation after seeding to allow cell attachment and migration; the total assay durations were therefore comparable across experiments.

Transwell assay

For the invasion assay, Transwell inserts (8-μm pore size) were pre-coated with Matrigel (Corning, USA). After 48 h of treatment, cells were seeded into upper chambers in serum-free medium, with complete medium containing 10% FBS in the lower chamber. After 24 h, invading cells were fixed, stained with 0.1% crystal violet, and counted under an IX51 microscope (Olympus, Japan).

Wound healing assay

After 48 h of treatment, cells were reseeded into 6-well plates and cultured until approximately 80% confluence. A straight scratch was created using a sterile 200 μL pipette tip. After washing with 1×PBS to remove detached cells, serum-free medium was added. The wound area was photographed immediately (0 h) and after 24 h of culture under an IX51 microscope. The relative wound closure was quantified using ImageJ software (NIH, USA).

RNA pull-down

DNA templates for in vitro transcription were generated by PCR from cDNA using specific primers. The sense RNA probe (positive) and antisense RNA probe (negative control) were transcribed in vitro using the T7 RNA polymerase system (Promega) and biotin-labeled using the Biotin RNA Labeling Mix (Roche). Biotinylated RNA probes (3 μg) were incubated with streptavidin magnetic beads (Invitrogen) to form probe-bead complexes. Whole-cell lysates from MDA-MB-231 and BT-549 cells were then incubated with the RNA-bound beads at 4°C for 2 h. After extensive washing, the bound proteins were eluted and analyzed by silver staining and subsequent mass spectrometry (LC-MS/MS). The primers used for probe generation were as follows: LINC00294-Sense (F: 5'-TAATACGACTCACTATAGGGGCCAGAAGACCCTCATCCAT-3'; R: 5'-GGCCCGTAAAATGTGCTTGA-3') and LINC00294-Antisense (F: 5'-GCCAGAAGACCCTCATCCAT-3'; R: 5'-TAATACGACTCACTATAGGGGGCCCGTAAAATGTGCTTGA-3'). This experiment was conducted by Jiangsu KeyGEN Biotechnology Co., Ltd. (Nanjing, China). RNA pull-down followed by mass spectrometry identifies candidate RNA-associated proteins and does not by itself distinguish direct from indirect interactions; candidate proteins were therefore subjected to functional validation rather than interpreted as direct binders.

mRNA-seq

mRNA-seq was conducted by KeyGEN BioTECH (Nanjing, China). Total RNA was extracted from cells in the NC, LINC00294-overexpression,

and LINC00294/CSTF1 co-overexpression groups using TRIzol reagent (Invitrogen) and assessed for integrity (RIN > 7.0) using an Agilent 2100 Bioanalyzer. Libraries were constructed with the NEBNext Ultra II RNA Library Prep Kit and sequenced on an Illumina NovaSeq 6000 platform (paired-end 150 bp). Raw reads were processed with fastp, aligned to the human reference genome (GRCh38) using HISAT2, and quantified as FPKM with StringTie. Differential expression analysis was performed using DESeq2 ($|\log_2 FC| > 1$, adjusted $P < 0.05$). GO and KEGG enrichment analyses were conducted using clusterProfiler.

Malondialdehyde (MDA), glutathione (GSH), and oxidized glutathione (GSSG) assays

Intracellular MDA, GSH, and GSSG levels were measured using commercial colorimetric assay kits (Beyotime) according to the manufacturer's instructions. After 48 h of treatment, cells were harvested and lysed. Absorbance was measured using a Spark microplate reader (Tecan, Switzerland), and results were normalized to total protein content.

Total RNA extraction and real-time quantitative PCR (RT-qPCR)

Total RNA was isolated from cultured cells using TRIzol reagent (Invitrogen) following the manufacturer's protocol. RNA concentration and purity were assessed using a UV spectrophotometer (Shimadzu, UV-2450). Reverse transcription was then performed to synthesize cDNA using a commercial first-strand synthesis kit (TaKaRa). The qPCR reactions were carried out in a 20 μL reaction mixture containing 10 μL of 2× TB Green Premix Ex Taq II (TaKaRa), 2 μL each of forward and reverse primers (10 μM), 1 μL of cDNA template, and 7 μL of 0.1% RNase-free water. The amplification protocol on an ABI StepOne Plus Real-Time PCR system consisted of an initial denaturation at 95°C for 5 min, followed by 40 cycles of 95°C for 20 s, 60°C for 20 s, and 72°C for 20 s. The expression levels of LINC00294, *CSTF1*, *TAGLN*, *TIMP3*, *CCL20*, and *LCN2* were analyzed with three biological replicates, each comprising three technical replicates. The relative mRNA expression was calculated using the $2^{-\Delta\Delta Ct}$ method, with GAPDH as the endogenous control. The primer sequences are listed in Table S2 and were synthesized by KeyGEN BioTECH.

Animal model

Female BALB/c nude mice (6-8 weeks old) were purchased from Hangzhou Ziyuan Experimental Animal Technology Co., Ltd. (SCXK (Zhe) 2024-0004) with the animal experiment protocol approved by the Animal Welfare and Ethics Committee of Dalian Medical University (Ethical Number: L250804280). Mice were acclimatized for one week under specific pathogen-free conditions (20-26°C, 40-70% humidity, 12 h light/dark cycle) in ventilated polycarbonate cages (≤ 5 mice/cage) with free access to feed and drinking water. MDA-MB-231 cells in logarithmic growth phase were resuspended in sterile PBS at 1×10^7 cells/mL, and 0.1 mL (1×10^6 cells) was subcutaneously injected into the right flank of each mouse. When tumor volume reached 80-100 mm^3, mice were randomized into three groups (n = 5) using a computer-generated random-number table, with balanced baseline tumor volumes across groups, by an investigator who was not involved in subsequent outcome measurements: Model, LV-LINC00294, and LV-LINC00294 + LV-CSTF1. Tumor-dimension measurements and the histopathological and Western blot quantifications were performed by investigators blinded to the group allocation. Lentiviral stock solutions (20 μL per mouse, constructed by KeyGEN BioTECH) were administered by intratumoral injection once every 3 days. Body weight was measured every 3 days on days 1, 4, 7, 10, 13, 16, 19, and 22 (8 timepoints) using an electronic balance, and tumor dimensions were measured every 3 days from day 7 (days 7, 10, 13, 16, 19, and 22; 6 timepoints) using a digital caliper; tumor volume was calculated as $V = 0.5\times L\times W^2$ (L, longest diameter; W, shortest diameter). After the 21-day intervention, mice were euthanized on day 22 by CO_2 asphyxiation followed by cervical dislocation. Tumors were dissected, adjacent skin and connective tissue were removed, and wet weight was recorded. Each tumor was divided into three portions on ice: (I) 50-100 mg was passed through a 40-μm cell strainer to generate a single-cell suspension for immediate flow cytometry analysis; (II) a 5 mm × 5 mm × 3 mm block was fixed in 4% paraformaldehyde for 24 h and then transferred to 70% ethanol at 4°C for HE staining; (III) 100-200 mg was snap-frozen in liquid nitrogen and stored at -80°C for Western blot analysis.

Flow cytometry

Cells were collected, washed with PBS, and resuspended in 500 μL binding buffer. Annexin V-APC (5 μL) and 7-AAD (5 μL) (KeyGEN BioTECH) were added to the cell suspension, followed by incubation at room temperature for 15 min in the dark. Samples were acquired within 1 h using a CytoFLEX flow cytometer (Beckman Coulter, USA). A minimum of 10,000 cells per sample were analyzed. Data were analyzed using FlowJo software, and cells were classified as viable (Annexin V^-/7-AAD^-), early apoptotic (Annexin V^+/7-AAD^-), late apoptotic (Annexin V^+/7-AAD^+), or necrotic/damaged (Annexin V^-/7-AAD^+).

Lipid peroxides (LPO) assay

LPO levels in cells and tumor tissues were measured using the BODIPY™ 581/591 C11 probe (Thermo Fisher Scientific). Cells were treated for 48 h, harvested, and incubated with C11-BODIPY™ in serum-free medium at 37°C for 30 min in the dark. Tumor tissues were enzymatically digested into single-cell suspensions and incubated with C11-BODIPY™. Intracellular lipid peroxidation was quantified using a CytoFLEX flow cytometer (Beckman Coulter, USA).

Fe^{2+} assay

Fe^{2+} levels were detected using the FerroOrange fluorescent probe (Dojindo, Japan). For cells, cells were seeded on coverslips and treated for 48 h, followed by incubation with 1 μM FerroOrange at 37°C in the dark for 30 min. Fluorescence images were acquired using an IX51 fluorescence microscope (Olympus, Japan). For tumor tissues, single-cell suspensions were prepared and incubated with 1 μM FerroOrange under identical conditions, and Fe^{2+} levels were quantified using a CytoFLEX flow cytometer (Beckman Coulter, USA).

Hematoxylin-eosin (HE) staining and terminal deoxynucleotidyl transferase dUTP nick-end labeling (TUNEL) assay

For histopathological analysis, fixed tumor tissues were dehydrated through a graded ethanol series, cleared in xylene, and embedded in paraffin. Serial 4-μm-thick sections were cut and mounted on glass slides for HE staining and TUNEL assay (KeyGEN BioTECH). For HE staining, deparaffinized and rehydrated sections were stained with hematoxylin for 5 min, differentiated in 1% acid-alcohol, counterstained with eosin for 3 min, dehydrated, cleared, mounted with neutral balsam, and observed under a light microscope to assess tumor morphology, necrosis, and pathological changes. For TUNEL assay, deparaffinized and rehydrated sections were treated with 20 μg/mL proteinase K at 37°C for 20 min, rinsed with PBS, incubated with TUNEL reaction mixture in the dark at 37°C for 60 min, counterstained with DAPI, and sealed with anti-fade mounting medium. Apoptotic cells were quantified under a fluorescence microscope, and the apoptotic index was calculated as the percentage of TUNEL-positive cells relative to total DAPI-stained cells.

Western blot

Total proteins were extracted using a Whole Cell Lysis Assay Kit (KeyGEN BioTECH). Protein concentration was determined using a BCA protein assay kit (KeyGEN BioTECH). Equal amounts of protein (20 μg) were separated by SDS-PAGE. After electrophoresis, proteins were transferred to PVDF membranes. The membranes were blocked with 5% non-fat milk in TBST for 1 h at room temperature and then incubated overnight at 4°C with the following primary antibodies listed in Table S3. Following primary antibody incubation, the membranes were washed with TBST and then incubated with the secondary antibodies (also listed in Table S3) at room temperature for 1.5 h. Protein bands were visualized using an enhanced chemiluminescence detection system (KeyGEN BioTECH), and images were captured with a chemiluminescence imaging system (Bio-Rad, USA).

Statistical analysis

Data are presented as mean ± standard deviation. Statistical analyses were performed using SPSS version 25.0, and graphs were generated with GraphPad Prism version 9.0. For the paired tumor and adjacent normal tissues (n = 11 pairs), a paired-samples t-test was used. Normality and homogeneity of variance were assessed using Shapiro-Wilk and Levene's tests, respectively; given the small sample size (n = 3) of the in vitro experiments, the power of

the Shapiro-Wilk normality test is inherently limited, and the results of parametric tests were therefore interpreted with caution. For data satisfying both assumptions, an independent-samples t-test was used for comparisons between two groups, while one-way ANOVA followed by the Tukey post-hoc test was used for multiple comparisons. For data violating the normality assumption, the Kruskal-Wallis test with Dunn's post-hoc test was applied. For data that were normally distributed but violated the homogeneity of variance assumption, Welch's ANOVA followed by the Games-Howell test was used. For longitudinally measured tumor volume and body weight in the xenograft experiment, differences were analyzed by two-way repeated-measures ANOVA with time as the within-subject factor and treatment group as the between-subject factor, followed by the Bonferroni post-hoc test; Greenhouse-Geisser correction was applied when the sphericity assumption was violated (Mauchly's test). Tumor weight at the endpoint was compared among groups by one-way ANOVA followed by the Tukey post-hoc test. *P* values < 0.05 were considered statistically significant.

The RNA pull-down coupled with mass spectrometry, mRNA sequencing, and construction of stable cell lines were performed by Jiangsu KeyGEN Biotechnology Co., Ltd. (Nanjing, China) under the supervision of the authors. The authors confirm that all primary data, including raw sequencing reads, mass spectrometry spectra, and original images, were generated for this study, have been obtained from the commercial provider, and have been independently verified and analyzed by the authors, who take full responsibility for the integrity of the data.

Results

LINC00294 is downregulated in TNBC and its overexpression inhibits cell proliferation, invasion, migration, and induces apoptosis

To explore the association between LINC00294 and TNBC pathogenesis, LINC00294 expression levels were quantified in TNBC tissues and matched adjacent non-tumor tissues. The results demonstrated a marked downregulation of LINC00294 in tumor tissues compared with adjacent non-tumor tissues ($P < 0.05$, **Figure 1A**). Consistently, TNBC cell lines (MDA-MB-231 and BT-549) exhibited significantly lower LINC00294 expression than the normal mammary epithelial cell line MCF-10A ($P < 0.05$, **Figure 1B**), suggesting an inverse correlation between LINC00294 abundance and TNBC progression. Functional assays revealed that overexpression of LINC00294 significantly suppressed proliferation ($P < 0.001$) and promoted apoptosis ($P < 0.001$) in MDA-MB-231 and BT-549 cells (**Figure 1C-E**). More importantly, LINC00294 overexpression substantially attenuated the invasive and migratory capacities of both TNBC cell lines ($P < 0.001$, **Figure 1F** and **1G**). Collectively, these findings establish LINC00294 as a TNBC-suppressive lncRNA, whose downregulation unleashes proliferative, anti-apoptotic, and metastatic programs, thereby accelerating TNBC progression.

LINC00294 may exert its tumor-suppressive function through interaction with CSTF1

To investigate the potential mechanism by which LINC00294 regulates the proliferation, apoptosis, invasion, and migration of TNBC cells, RNA pull-down combined with mass spectrometry was used to identify proteins interacting with LINC00294. The silver staining results showed that LINC00294 binds to several specific protein bands (**Figure 2A**). In MDA-MB-231 cells, 381 candidate LINC00294-associated proteins were identified (**Figure 2B**), which were primarily enriched in KEGG pathways including motor proteins, endocytosis, and ATP-dependent chromatin remodeling (**Figure 2D**). In BT-549 cells, 581 candidate LINC00294-associated proteins were identified (**Figure 2C**), with predominant enrichment in KEGG pathways such as endocytosis, Huntington's disease, and Parkinson's disease (**Figure 2E**). To screen for key LINC00294-interacting proteins, proteins with #Unique ≥ 2 were selected, and a Venn diagram was used to identify overlapping proteins between the two cell lines (**Figure 2F**). CSTF1 was the only overlapping protein identified in both cell lines. Because RNA pull-down/MS identifies candidate interactors without providing direct evidence of physical binding, CSTF1 was prioritized for functional validation rather than interpreted as a direct binder. CSTF1 is involved in pre-mRNA polyadenylation and 3'-end cleavage. Analysis of the Cancer Genome

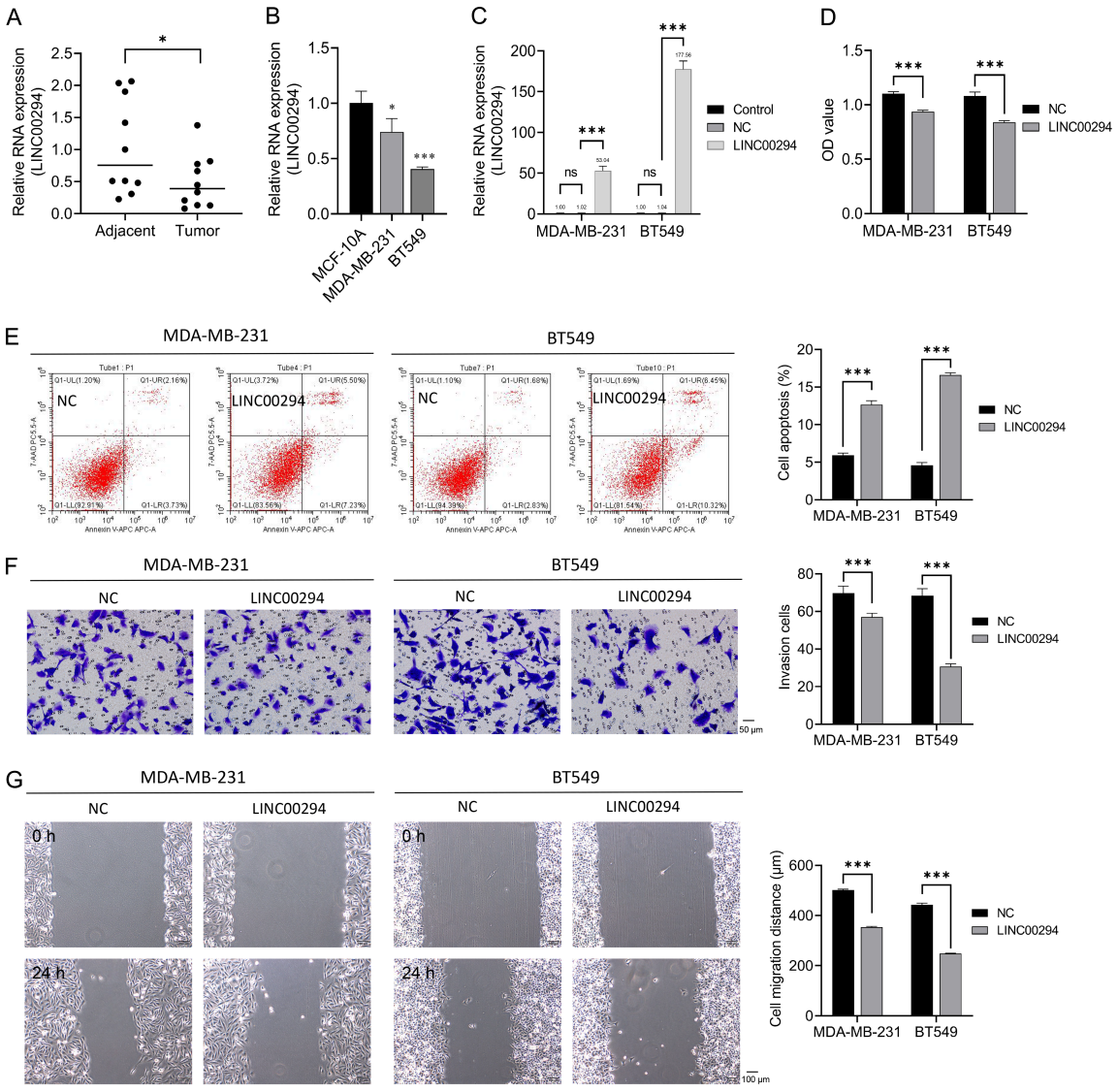

Figure 1. LINC00294 functions as a tumor suppressor in TNBC by inhibiting proliferation, migration, invasion, and inducing apoptosis. (A) RT-qPCR analysis of LINC00294 expression in tumor tissues and paired adjacent normal tissues from TNBC patients. (B) RT-qPCR analysis of LINC00294 expression in indicated cell lines. (C) RT-qPCR validation of LINC00294 overexpression in stable transfected cell lines. (D) CCK-8 assay for cell proliferation. (E) Annexin V-APC/7-AAD flow cytometric analysis of cell apoptosis. (F) Cell invasion was assessed by Transwell assay (200×). Scale bar = 50 μm. (G) Cell migration was evaluated by wound healing assay (100×). Scale bar = 100 μm. Data are presented as mean ± SD (n = 3, except in A where n = 11 paired samples); statistical significance for (A) was determined by a paired-samples t-test. **P* < 0.05, ***P* < 0.01, ****P* < 0.001.

Atlas (TCGA) database indicated that CSTF1 is highly expressed in breast cancer (**Figure 2G**), implying that CSTF1 may function as an oncogene in breast cancer progression. It has been reported that lncRNAs can act as RNA-binding protein (RBP) sponges, interfering with the regulatory effects of RBPs on downstream targets. Thus, LINC00294 may associate with CSTF1, thereby attenuating its oncogenic activity and promoting tumor cell apoptosis.

LINC00294 exerts its tumor-suppressive effect by antagonizing CSTF1

To investigate whether CSTF1 mediates the tumor-suppressive effects of LINC00294, the effects of CSTF1 overexpression alone or in combination with LINC00294 overexpression on cell proliferation, apoptosis, invasion, and migration were analyzed. CSTF1 overexpression promoted TNBC cell proliferation and inhibited apoptosis, but these effects were

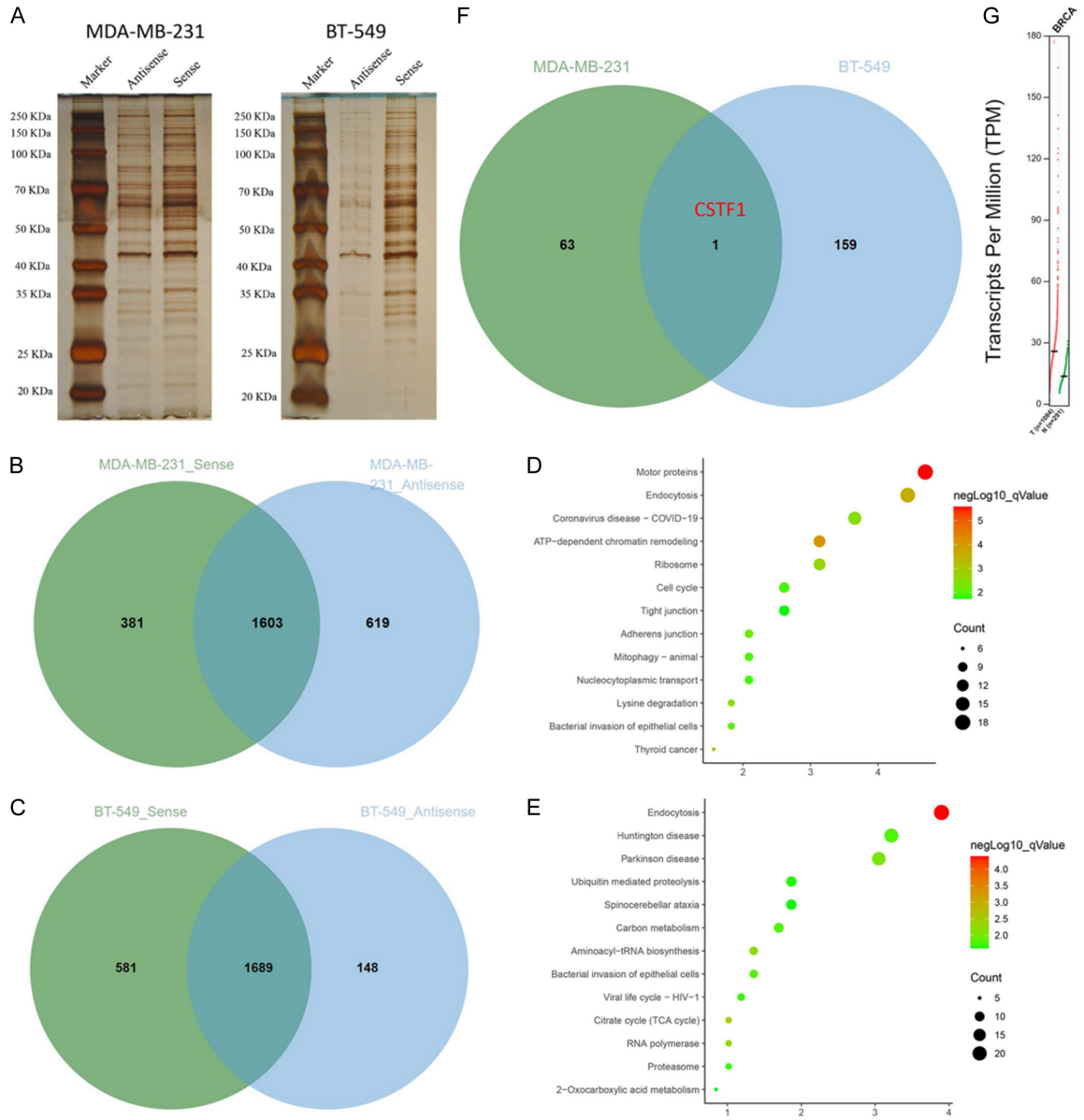

Figure 2. Identification of proteins interacting with LINC00294. A. Silver staining of protein bands bound to LINC00294. B, C. Screening of proteins specifically interacting with LINC00294 via Venn diagrams in MDA-MB-231 and BT-549 cells. D. KEGG enrichment analysis of the candidate LINC00294-associated proteins identified by RNA pull-down/MS in MDA-MB-231 cells (exploratory; no input/background normalization). E. KEGG enrichment analysis of the candidate LINC00294-associated proteins in BT-549 cells (exploratory; no input/background normalization). F. Venn diagram showing overlapping proteins between the two cell lines. G. Expression of CSTF1 in breast cancer and adjacent normal tissues based on the TCGA database.

reversed by LINC00294 overexpression (**Figure 3A-D**). Furthermore, CSTF1 overexpression enhanced TNBC cell migration and invasion, and these malignant phenotypes were similarly abrogated by LINC00294 overexpression (**Figure 3E** and **3F**). These findings confirm that LINC00294 functionally antagonizes CSTF1-mediated oncogenic effects.

LCN2 is a candidate downstream target of the LINC00294/CSTF1 axis

To elucidate the downstream targets and pathways regulated by the LINC00294/CSTF1 axis, mRNA-seq was performed to screen for downstream effectors (**Figure 4A**). Compared with the control group, LINC00294 overexpression

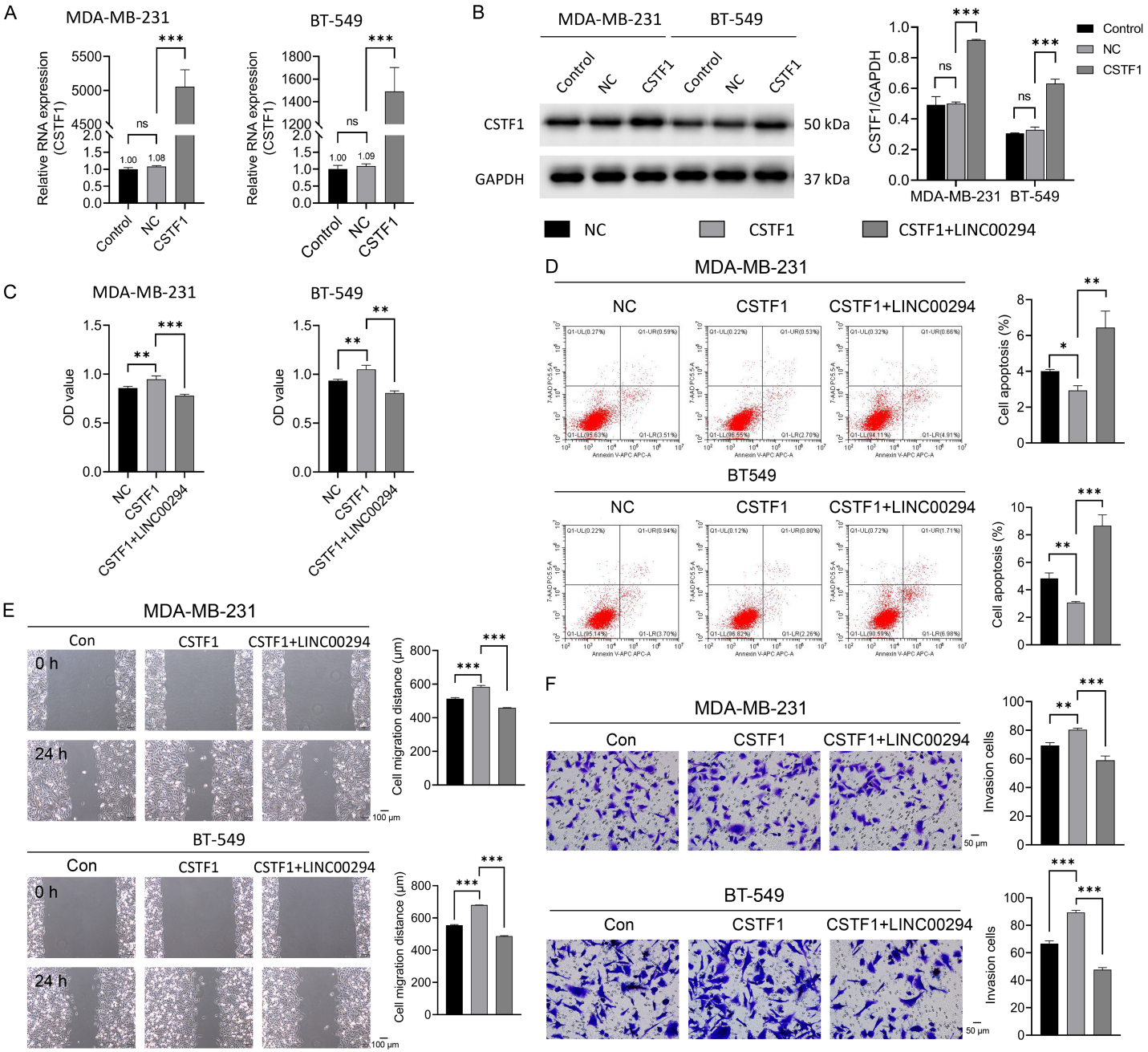
A
MDA-MB-231
BT-549
Relative RNA expression (CSTF1)
Control
NC
CSTF1
ns
***
B
MDA-MB-231
BT-549
Control
NC
CSTF1
CSTF1
GAPDH
50 kDa
37 kDa
CSTF1/GAPDH
NC
CSTF1
CSTF1+LINC00294
C
MDA-MB-231
BT-549
OD value
NC
CSTF1
CSTF1+LINC00294
**
D
MDA-MB-231
BT549
NC
CSTF1
CSTF1+LINC00294
Cell apoptosis (%)
E
MDA-MB-231
BT-549
Con
CSTF1
CSTF1+LINC00294
0 h
24 h
Cell migration distance (μm)
100 μm
F
MDA-MB-231
BT-549
Con
CSTF1
CSTF1+LINC00294
Invasion cells
50 μm

Figure 3. LINC00294 functionally antagonizes CSTF1 to inhibit proliferation, migration, and invasion, and promote apoptosis in TNBC cells. A. RT-qPCR analysis of CSTF1 mRNA expression in TNBC cells. B. CSTF1 protein expressions were detected by Western blot. C. CCK-8 assay for cell proliferation. D. Annexin V-APC/7-AAD assay of cell apoptosis. E. Cell migration was evaluated by wound healing assay (100×). Scale bar = 100 μm. F. Cell invasion was assessed by Transwell assay (200×). Scale bar = 50 μm. Data are presented as mean ± SD (n = 3). *$P < 0.05$, **$P < 0.01$, ***$P < 0.001$.

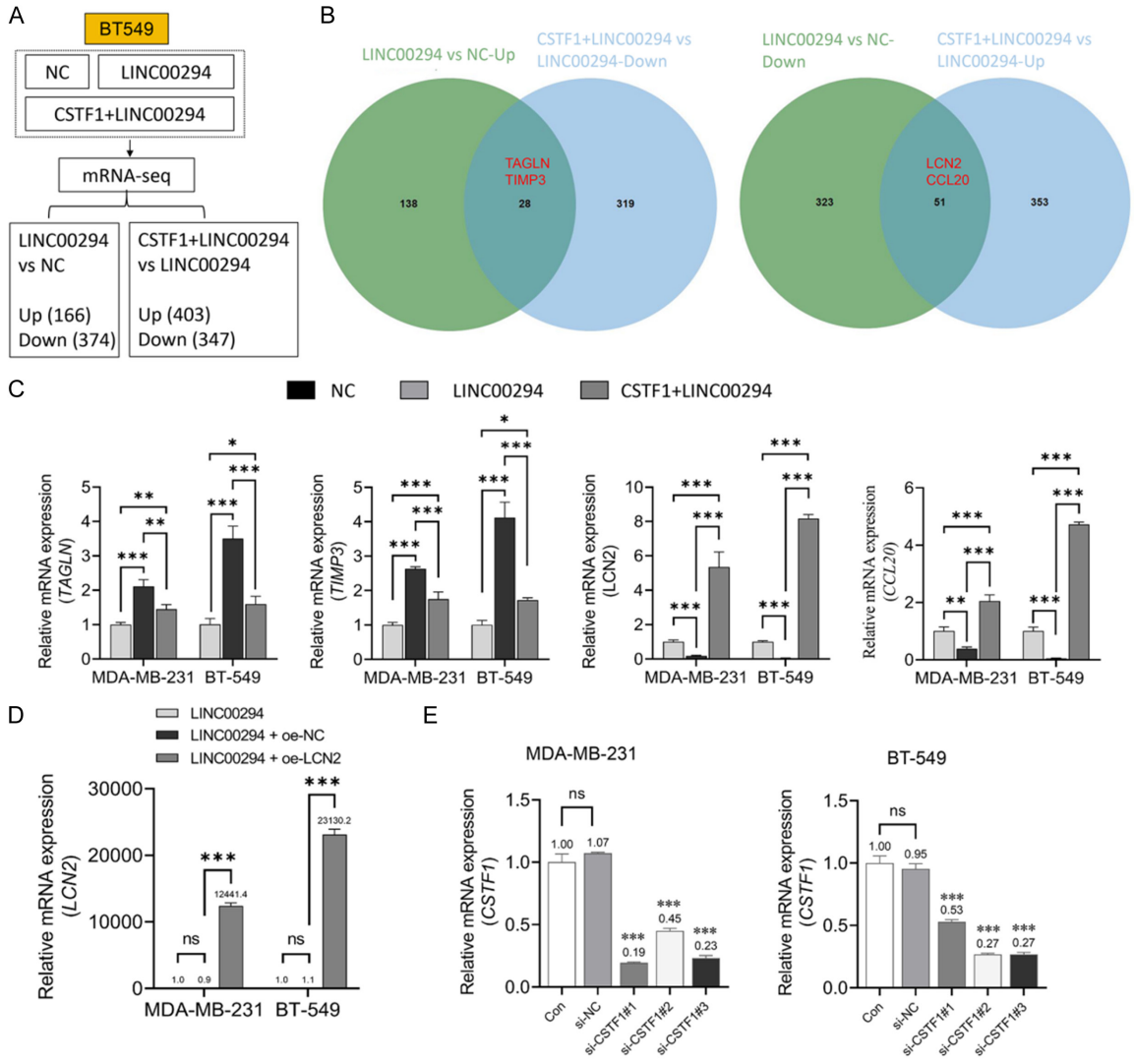

Figure 4. LCN2 is a downstream target of the LINC00294/CSTF1 axis. A. Schematic diagram of mRNA-seq. B. Venn diagram of differentially expressed genes. C. RT-qPCR validation of the four candidate genes (TAGLN, TIMP3, LCN2, and CCL20) in MDA-MB-231 and BT-549 cells among the NC, LINC00294-overexpression, and CSTF1 + LINC00294 groups. D. RT-qPCR validation of LCN2 overexpression efficiency. E. RT-qPCR validation of CSTF1 siRNA knockdown efficiency. Data are presented as mean ± SD (n = 3). *$P < 0.05$, **$P < 0.01$, ***$P < 0.001$, vs si-NC.

significantly upregulated 166 genes and downregulated 374 genes; in the combined overexpression group (LINC00294 + CSTF1), 403 genes were significantly upregulated and 347 genes were downregulated relative to the LINC00294 overexpression group alone (**Figure 4A** and S1A, S1B). KEGG enrichment analysis revealed that differentially expressed genes (DEGs) between the control and LINC00294 overexpression groups were mainly enriched in the PI3K/AKT signaling pathway, pathways in cancer, and cytokine-cytokine receptor interaction. DEGs between the LINC00294 overexpression and combined overexpression groups

were primarily enriched in pathways in cancer, MAPK signaling, cytokine-cytokine receptor interaction, and TNF signaling (Figure S1C).

From the intersection of these transcriptional programs, we prioritized four candidate effectors - *TAGLN*, *TIMP3*, *LCN2*, and *CCL20* - that exhibited antagonistic regulation by LINC00294 and CSTF1 (**Figure 4B**). RT-qPCR validation confirmed the antagonistic regulation of all four candidates (**Figure 4C**): LINC00294 overexpression upregulated TAGLN and TIMP3 but downregulated LCN2 and CCL20, whereas combined CSTF1 overexpression reversed each of these changes. LCN2 was prioritized for subsequent functional validation given that it has been reported to exert oncogenic functions in breast cancer and to suppress ferroptosis [15, 16]. To functionally interrogate this axis, we constructed an LCN2 overexpression plasmid, which significantly elevated LCN2 mRNA levels upon transfection ($P < 0.001$, **Figure 4D**). Additionally, we screened three independent CSTF1-targeting siRNAs and selected si-CSTF1#3, which achieved the most efficient knockdown in both cell lines, for subsequent mechanistic studies (**Figure 4E**).

The LINC00294/CSTF1 axis inhibits cell proliferation, migration, and invasion while promoting apoptosis, potentially through LCN2-mediated ferroptosis resistance

Having identified LCN2 as a candidate downstream target of the LINC00294/CSTF1 axis, we next investigated whether the tumor-suppressive effects of LINC00294 involve alleviation of LCN2-mediated ferroptosis resistance - ferroptosis being a form of iron-dependent lipid peroxidative cell death with emerging therapeutic relevance in oncology [17]. Under LINC00294-overexpressing conditions, ectopic LCN2 expression significantly promoted cell proliferation and suppressed apoptosis; however, these oncogenic effects were completely reversed by either CSTF1 knockdown or pharmacological induction of ferroptosis with erastin (**Figure 5A** and **5B**). Concordantly, LCN2-enhanced invasive and migratory phenotypes were similarly attenuated by CSTF1 silencing or erastin treatment (**Figure 6A** and **6B**).

More importantly, LCN2 overexpression decreased intracellular Fe^{2+} levels and LPO production while increasing the GSH/GSSG ratio, all of which were reversed by CSTF1 knockdown or erastin treatment (**Figure 7A-C**). The decrease in MDA content induced by LCN2 overexpression was also reversed by CSTF1 knockdown or erastin (**Figure 8A**). Key ferroptosis-related proteins, including acyl-CoA synthetase long-chain family member 4 (ACSL4), ferroptosis suppressor protein 1 (FSP1), and glutathione peroxidase 4 (GPX4), were significantly altered following LCN2 overexpression: ACSL4 expression was downregulated, whereas FSP1 and GPX4 expression were upregulated. These changes were again reversed by CSTF1 knockdown or erastin treatment (**Figure 8B-D**). Together, these results suggest that LINC00294 suppresses TNBC malignant progression in part through LCN2-associated modulation of ferroptosis. LCN2 confers ferroptosis resistance by maintaining intracellular redox homeostasis and suppressing lipid peroxidation and iron accumulation. Consistent with a regulatory model, LINC00294 functionally antagonizes CSTF1, and this antagonism is associated with reduced LCN2 expression and restored ferroptosis.

The LINC00294/CSTF1 axis inhibits xenograft tumor growth in association with ferroptosis induction

To assess the in vivo relevance of our mechanistic findings, we established subcutaneous TNBC xenograft models in nude mice. Representative images of the excised xenograft tumors from each group are shown in **Figure 9A**. As shown in **Figure 9B**, the body weight of mice in all three groups increased gradually over the 21-day observation period, with measurements obtained every 3 days on days 1, 4, 7, 10, 13, 16, 19, and 22 (8 timepoints). Two-way repeated-measures ANOVA with Greenhouse-Geisser correction showed that the main effect of time on body weight was statistically significant ($F(1.53, 18.34) = 1305.00$, $P < 0.001$), while there was no significant difference in body weight among the three groups ($F(2, 12) = 0.03$, $P = 0.966$). The time × group interaction did not reach the significance threshold ($F(14, 84) = 0.99$, $P = 0.468$), indicating consistent body weight growth trends across all groups. For tumor volume dynamics from day 7 onward (**Figure 9C**), two-way repeated-measures ANOVA demonstrated significant main effects of time ($F(1.04, 12.46) = 796.80$,

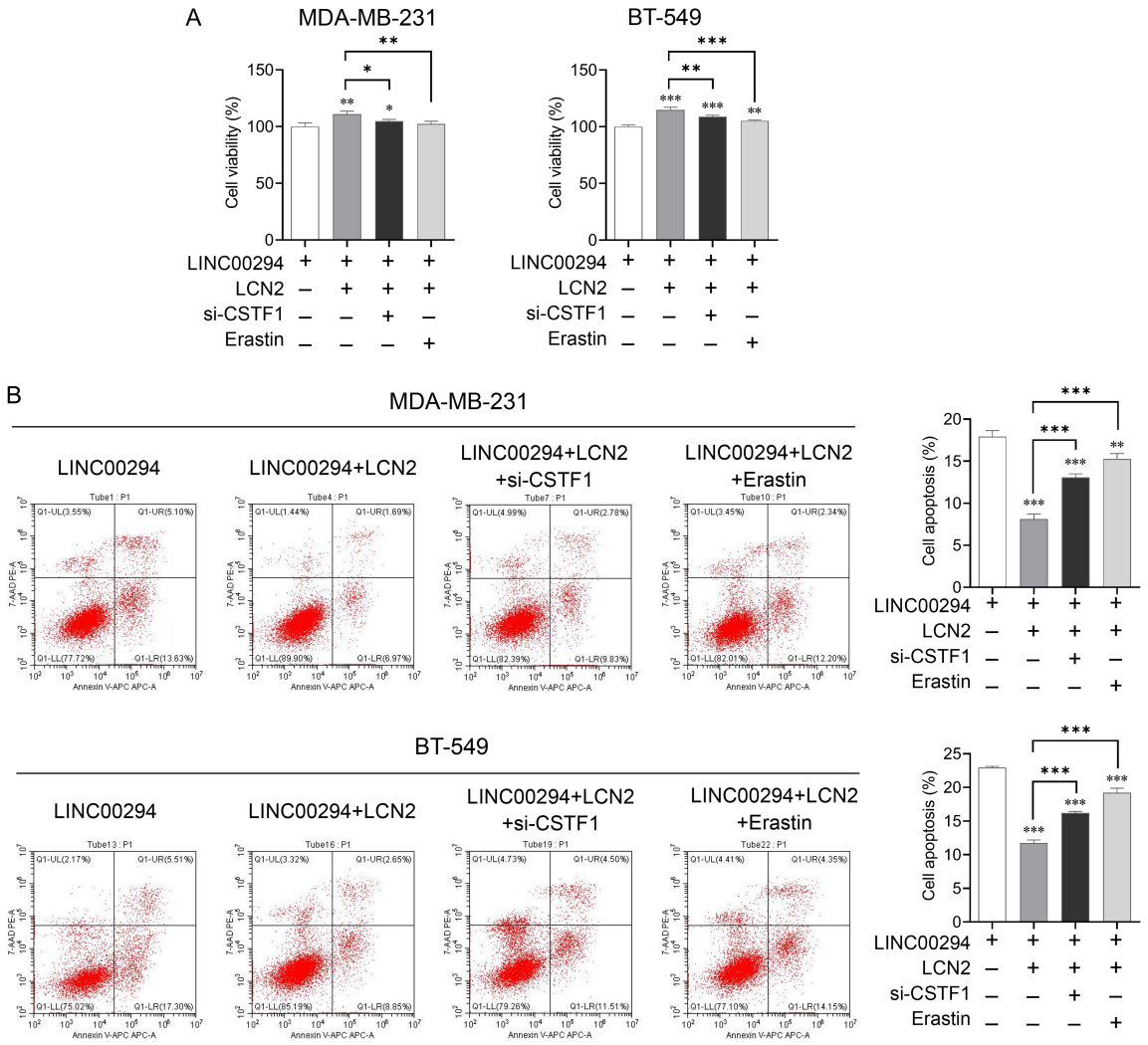

Figure 5. The LINC00294/CSTF1 axis inhibits cell proliferation while promoting apoptosis through LCN2-mediated ferroptosis. A. CCK-8 assay of cell proliferation. B. Annexin V-APC/7-AAD flow cytometric analysis of cell apoptosis. Data are presented as mean ± SD (n = 3). *P < 0.05, **P < 0.01, ***P < 0.001, vs LINC00294.

P < 0.001) and group (F (2, 12) = 47.67, P < 0.001), as well as a significant time × group interaction (F (10, 60) = 81.71, P < 0.001). Bonferroni post-hoc test at the endpoint (day 22) revealed that tumor volume in the LV-LINC00294 group was significantly smaller than that in the Model group (P < 0.001), whereas overexpression of CSTF1 significantly reversed the tumor-suppressive effect induced by LINC00294, as evidenced by the larger tumor volume in the LV-LINC00294 + LV-CSTF1 group compared with the LV-LINC00294 group (P < 0.01); the tumor volume of the LV-LINC00294 + LV-CSTF1 group remained significantly smaller than that of the Model group (P < 0.001). The endpoint tumor weight (**Figure 9D**) was significantly lower in the LV-LINC00294 group than in the Model group (P < 0.001), and this reduction was markedly attenuated in the LV-LINC00294 + LV-CSTF1 group (P < 0.01 vs. the LV-LINC00294 group). Histopathological examination revealed that control tumor cells maintained intact morphology with minimal necrosis or apoptosis. In stark contrast, LINC00294-overexpressing tumors exhibited extensive cellular shrinkage, cytoplasmic condensation, nuclear pyknosis, and widespread necrotic and apoptotic regions. These pathological changes were substantially attenuated when CSTF1 was simultaneously overexpressed (**Figure 9E** and **9F**). Further analyses of the xenograft tumors showed that LINC00294

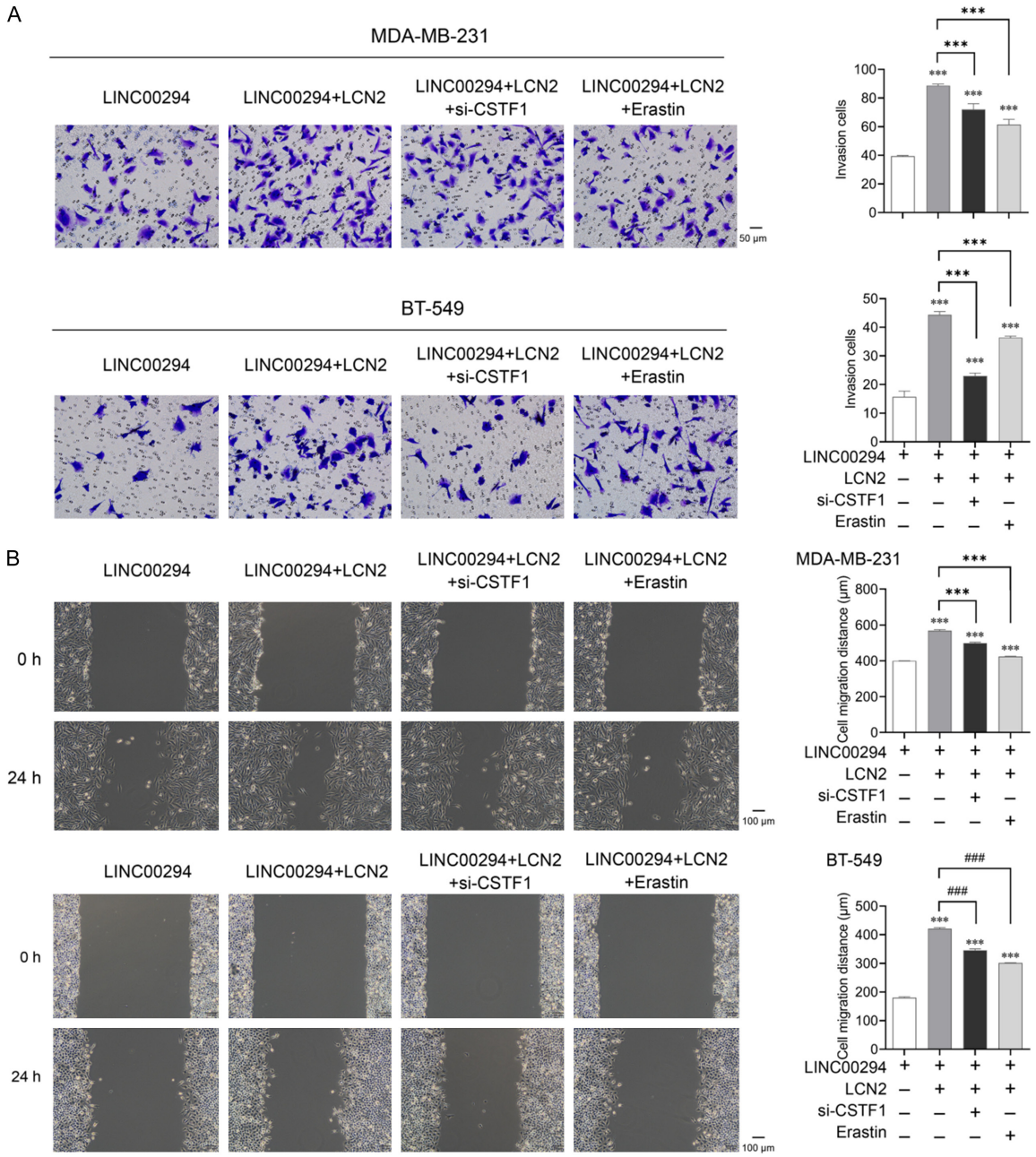

Figure 6. The LINC00294/CSTF1 axis inhibits cell invasion and migration through LCN2-mediated ferroptosis. A. Cell invasion was assessed by Transwell assay (200×). Scale bar = 50 μm. B. Cell migration was evaluated by wound healing assay (100×). Scale bar = 100 μm. Data are presented as mean ± SD (n = 3). ***$P < 0.001$, vs LINC00294; ###$P < 0.001$.

overexpression promoted the accumulation of intracellular Fe^{2+} and LPO, upregulated ACSL4 expression, and downregulated LCN2 and GPX4 expression. All these ferroptosis-promoting alterations were reversed by CSTF1 overexpression (**Figure 9G-I**). Collectively, these phenotypic findings indicate that intratumoral lentiviral delivery of LINC00294 exerted a tumor-suppressive effect in TNBC xenografts accompanied by ferroptosis-associated molecular and histopathological changes, and that CSTF1 co-overexpression antagonized these effects. Because transgene overexpression in the harvested tumors was not directly verified, these in vivo results should be interpreted as phenotypic evidence following lentiviral administration

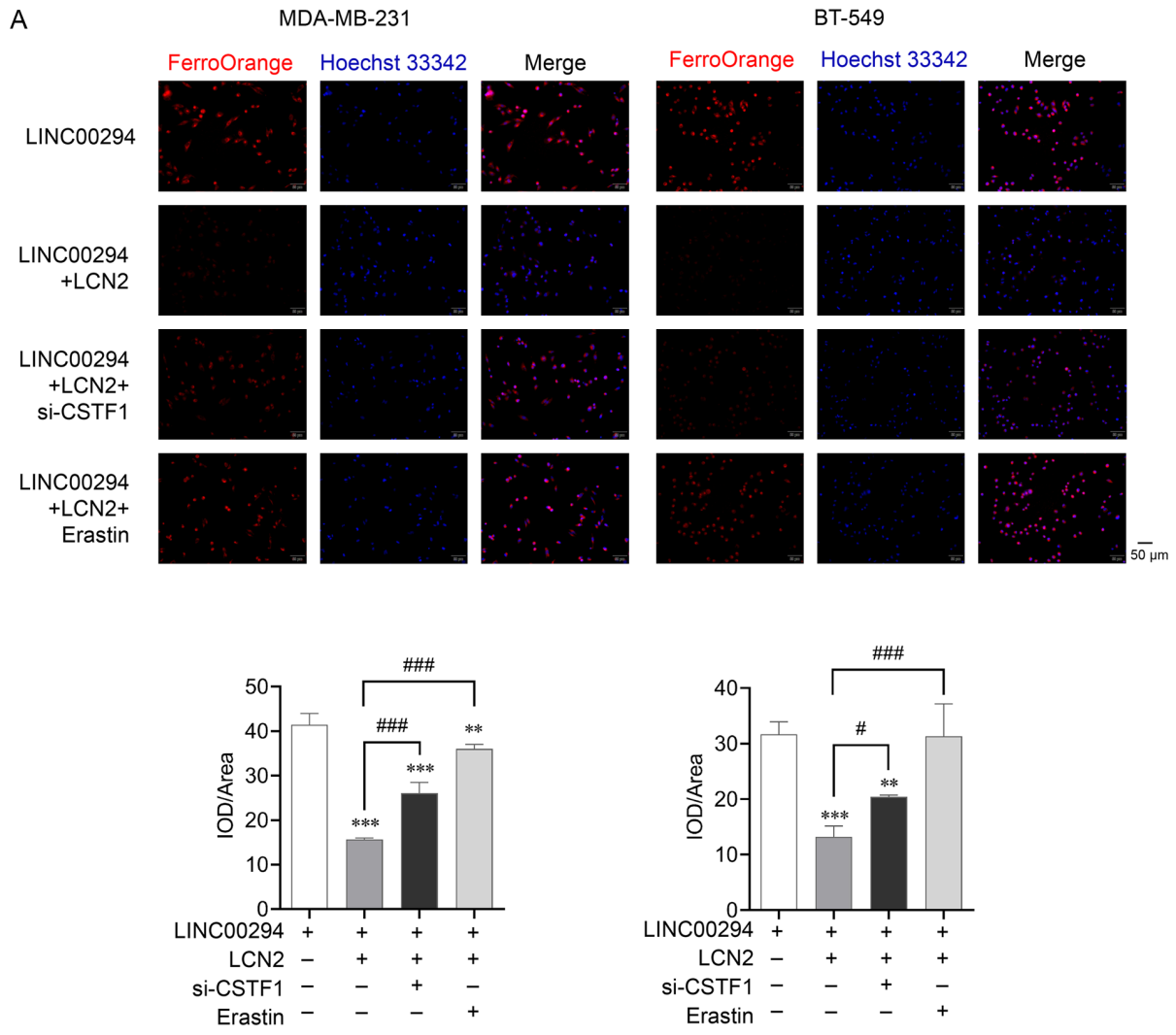
A
MDA-MB-231
BT-549
FerroOrange
Hoechst 33342
Merge
LINC00294
LINC00294 +LCN2
LINC00294 +LCN2+ si-CSTF1
LINC00294 +LCN2+ Erastin
50 μm
IOD/Area
LINC00294
LCN2
si-CSTF1
Erastin
C
MDA-MB-231
BT-549
GSH/GSSG

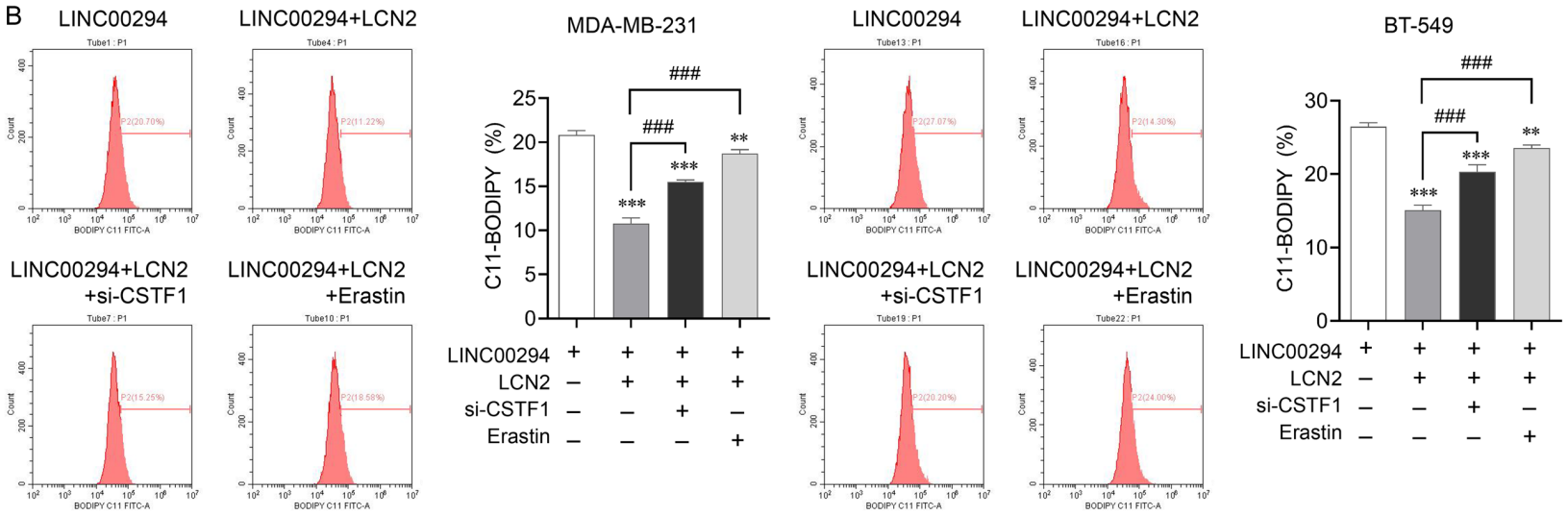

Figure 7. The LINC00294/CSTF1 axis promotes ferroptosis through LCN2. A. Intracellular Fe^{2+} levels were measured using the FerroOrange probe (200×). Scale bar = 50 μm. B. Intracellular lipid peroxidation was assessed with the C11-BODIPY probe. C. Changes in the GSH/GSSG ratio. Data are presented as mean ± SD (n = 3). $^{*}P < 0.05$, $^{**}P < 0.01$, $^{***}P < 0.001$, vs LINC00294; $^{\#\#}P < 0.01$, $^{\#\#\#}P < 0.001$.

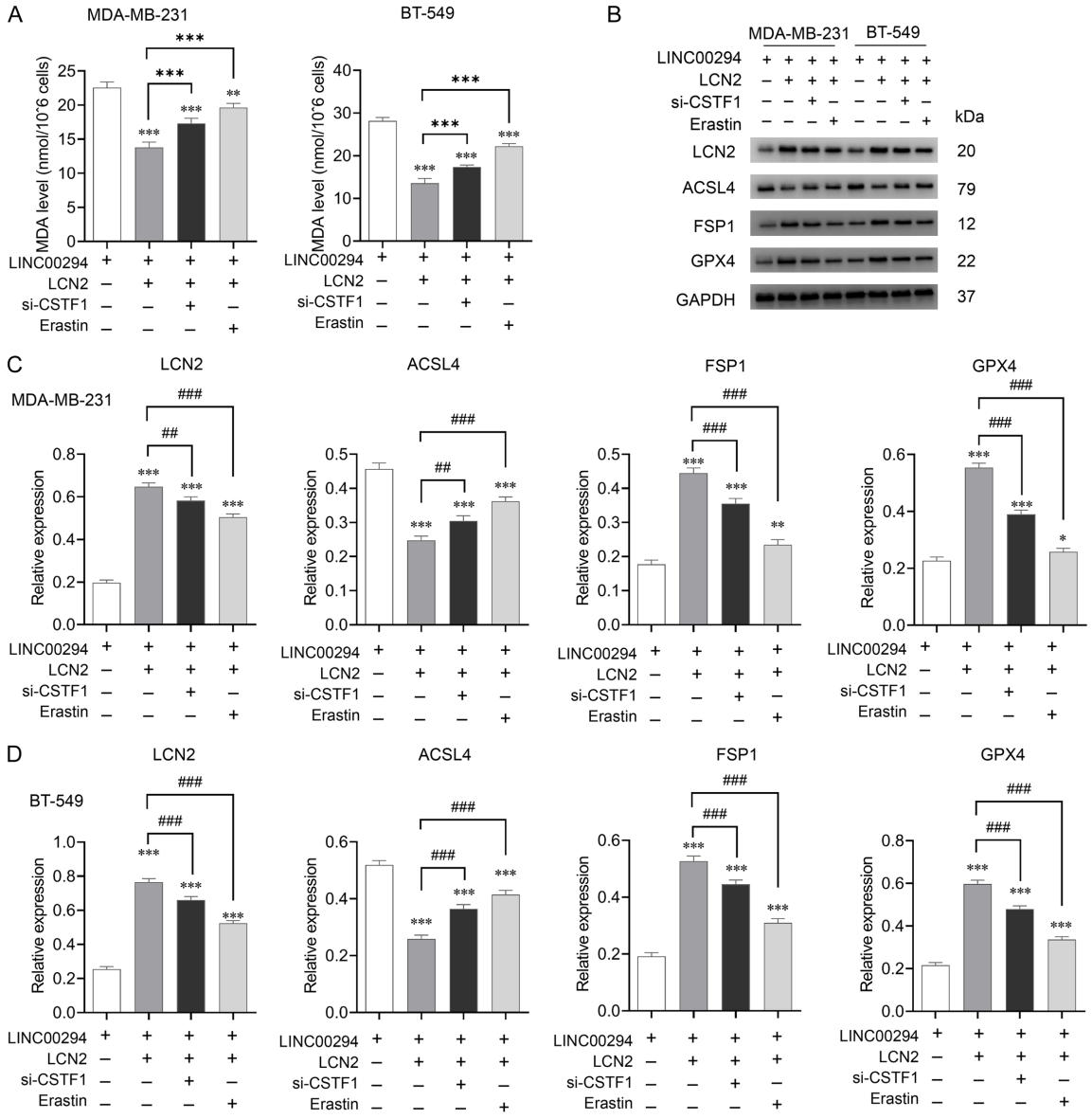

Figure 8. The LINC00294/CSTF1 axis promotes MDA production and regulates ferroptosis-related protein expression through LCN2. A. MDA levels. B. Representative Western blot images of ferroptosis-related proteins (LCN2, ACSL4, FSP1, and GPX4). C. Densitometric quantification of the Western blot bands in MDA-MB-231 cells. D. Densitometric quantification of the Western blot bands in BT-549 cells. Data are presented as mean ± SD (n = 3). $^{**}P < 0.01$, $^{***}P < 0.001$, vs LINC00294; $^{\#\#}P < 0.01$, $^{\#\#\#}P < 0.001$.

rather than as direct validation of the LINC00294/CSTF1-LCN2 regulatory mechanism.

Discussion

This study identifies a previously unrecognized regulatory node governing ferroptosis sensitivity in TNBC. We demonstrate that LINC00294, a downregulated LncRNA in TNBC, suppresses malignant progression by functionally antagonizing CSTF1, with reduced CSTF1-associated LCN2 expression and restored ferroptosis as candidate downstream events. These findings support a candidate LncRNA-binding protein-effector cascade that couples post-transcriptional control to cell death programs, with implications for TNBC-targeted therapy.

TNBC remains the most aggressive breast cancer subtype, lacking ER, PR, and HER2 expression and consequently devoid of approved targeted therapies [18]. The resulting high recur-

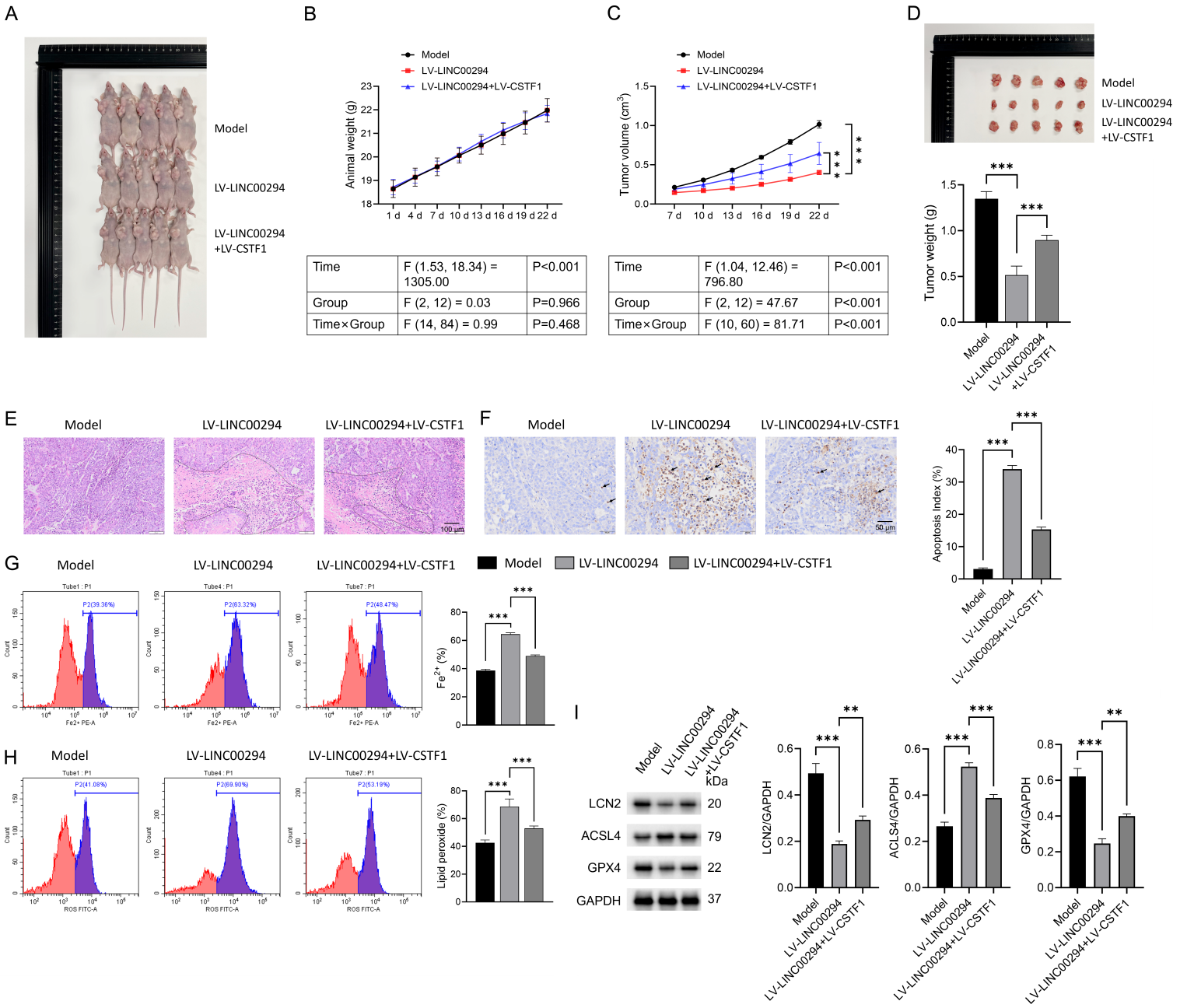

Time	F (1.53, 18.34) = 1305.00	P<0.001
Group	F (2, 12) = 0.03	P=0.966
Time×Group	F (14, 84) = 0.99	P=0.468

Time	F (1.04, 12.46) = 796.80	P<0.001
Group	F (2, 12) = 47.67	P<0.001
Time×Group	F (10, 60) = 81.71	P<0.001

Figure 9. The LINC00294/CSTF1 axis inhibits xenograft tumor growth in association with ferroptosis. A. Representative images of xenograft tumors. B. Changes in body weight of nude mice in each group during the intervention period (two-way repeated-measures ANOVA). C. Tumor volume was measured every 3 days from day 7 (days 7, 10, 13, 16, 19, and 22; 6 timepoints) and analyzed by two-way repeated-measures ANOVA (time×group) followed by the Bonferroni post-hoc test. D. Quantitative analysis of tumor weight in each group after euthanasia (one-way ANOVA followed by the Tukey post-hoc test). E. HE staining images of tumor tissues in each group (×100). Scale bar = 100 μm. F. TUNEL staining images of tumor tissues in each group (×200) and quantification of the apoptosis index. Scale bar = 50 μm. G. Detection of Fe^{2+} levels in tumor tissues by FerroOrange probe. H. Detection of lipid peroxide levels in tumor tissues by C11-BODIPY probe (flow cytometry) and quantitative analysis. I. Western blot of LCN2, ACSL4, and GPX4 in tumor tissues and densitometric quantification. Data are presented as mean ± SD (n = 5). **P < 0.01, ***P < 0.001.

rence and metastasis rates underscore an urgent need for mechanistic insights into TNBC biology [18, 19]. LncRNAs have emerged as critical regulators of cancer hallmarks, yet their specific roles in TNBC remain incompletely characterized [10, 11, 14, 20]. In this study, LINC00294 was found to be expressed at low levels in both tumor tissues and cancer cell lines. Its overexpression suppressed the proliferation, migration, and invasion of TNBC cells, suggesting an anti-cancer role in TNBC, which is consistent with the tumor-suppressive functions reported in colorectal cancer and glioma [10-12]. In contrast, oncogenic roles of LINC00294 have been described in cervical cancer and hepatocellular carcinoma [13, 14], highlighting that its function is highly context-dependent across tumor types. Moreover, the ability of LINC00294 to induce apoptosis in TNBC cells is particularly noteworthy, as apoptosis modulation is a critical aspect of enhancing the efficacy of existing treatment options and overcoming resistance to conventional therapies [21]. Notably, LINC00294 overexpression was well tolerated in nude mice, with no significant differences in body-weight gain among the groups; however, toxicity was not formally assessed by serum biochemistry or histopathology of major organs, and the safety profile requires further evaluation before any translational conclusions can be drawn.

In recent years, the interaction between lncRNAs and RBPs through “molecular sponge” or “decoy” mechanisms has attracted increasing attention in cancer research [22-25]. The binding of lncRNAs to RBPs plays a crucial role in post-transcriptional regulation, influencing the synthesis of cancer-related proteins by modulating mRNA stability. This, in turn, regulates the malignant biological behaviors of tumor cells, such as proliferation and metastasis, and plays an important role in therapeutic resistance [24]. In cervical cancer, lncRNA HOXA-AS2 binds to the Notch intracellular domain (NICD) to regulate the Notch pathway, exerting oncogenic effects in the development of cervical cancer [26]. In small cell lung cancer, lncRNA LYPLAL1-DT binds to the RBP ELAVL4, enhancing the stability of both LYPLAL1-DT and PFN2 mRNA, with upregulated PFN2 ultimately promoting tumorigenesis and invasion of small cell lung cancer [25]. In TNBC, it has also been found that lncRNA TMEM161B-AS1 interacts with RBFOX1, affecting the binding of RBFOX1 to SERPINB5 mRNA, ultimately inhibiting TNBC cell proliferation, migration, and invasion [22]. Interestingly, METTL3/YTHDC1-mediated N6-methyladenosine modification was significantly enriched in LINC00294 and shown to enhance its RNA stability. Additionally, LINC00294 promotes the interaction between YTHDC1 and HK2 as well as GLUT1 mRNA, ultimately leading to enhanced aerobic glycolysis in HCC cells [14]. Our RNA pull-down assays coupled with mass spectrometry identified CSTF1 as a candidate interactor of LINC00294 across two independent TNBC cell lines; however, because RNA pull-down does not formally demonstrate direct physical binding, independent validation by RIP-qPCR or RNA electrophoretic mobility shift assay will be required.

As a key component of the pre-mRNA 3’-end processing complex, CSTF1 has recently received increasing attention, and its oncogenic functions have been gradually uncovered [27]. A recent study reported that CSTF1 expression is elevated in HCC cases and closely correlated with multiple clinicopathological characteristics; increased CSTF1 expression is closely associated with various cancer-related pathways and the immune microenvironment [27]. Kaplan-Meier analysis showed that elevated CSTF1 expression predicts poor prognosis in

HCC patients [27]. TCGA database analysis revealed high CSTF1 expression in breast cancer tissues, consistent with our findings. Furthermore, through gain- and loss-of-function experiments, this study confirmed that CSTF1 overexpression significantly promotes TNBC cell proliferation and migration while inhibiting apoptosis in vitro, and abrogates the tumor-suppressive effect of LINC00294 in vivo. These findings establish the oncogenic role of CSTF1 in TNBC cells and the regulatory relationship between LINC00294 and CSTF1 both in vitro and in vivo.

To identify effector molecules executing the phenotypic output of the LINC00294/CSTF1 interaction, we performed transcriptome sequencing. LCN2 emerged as the candidate effector prioritized for further study, with LINC00294 negatively and CSTF1 positively regulating its expression. LCN2, also known as neutrophil gelatinase-associated lipocalin, has been implicated in promoting tumor cell survival, chemoresistance, and metastasis in breast cancer [15, 28, 29]. LCN2 is also established as a ferroptosis suppressor in breast cancer, where it chelates iron, limits lipid peroxidation, and maintains glutathione redox homeostasis [15, 16]. Our mechanistic dissection reveals that LCN2 overexpression recapitulates the CSTF1 oncogenic signature: reduced Fe^{2+}, diminished lipid peroxidation (MDA, C11-BODIPY), elevated GSH/GSSG ratio, and altered ferroptosis protein signatures. The upregulation of FSP1 and GPX4 is coherent with the established roles of these proteins as ferroptosis suppressors - GPX4 terminates lipid peroxidation cascades, whereas FSP1 inhibits ferroptosis in a glutathione-independent manner [30]. Critically, these anti-ferroptotic effects are abrogated by either CSTF1 knockdown or erastin treatment, positioning LCN2 as a putative functional mediator linking CSTF1 to ferroptosis resistance. Notably, Yao et al. reported the LIFR-NF-κB-LCN2 axis regulating ferroptosis sensitivity in liver cancer [17], suggesting that LCN2 is a ferroptosis gatekeeper molecule across different cancer types. This discovery provides a new perspective on the precision of ferroptosis regulation in TNBC and suggests that targeting LCN2 expression or its iron-chelation function may be an effective strategy for restoring chemotherapeutic sensitivity.

Several limitations warrant consideration. The in vivo validation was restricted to the MDA-MB-231 xenograft model; extension to additional TNBC cell lines and patient-derived xenograft models is needed to confirm generalizability. While our data support a functional link between CSTF1 and LCN2 expression, the precise mechanism remains undefined. CSTF1 is a core component of the pre-mRNA 3'-end cleavage and polyadenylation machinery and may regulate LCN2 through post-transcriptional mechanisms - such as alternative polyadenylation, mRNA stability, or nuclear export - rather than direct transcriptional activation. RIP-qPCR assays to assess CSTF1 binding to LCN2 pre-mRNA or mature transcript, and analysis of LCN2 mRNA half-life and polyadenylation site usage upon CSTF1 or LINC00294 manipulation, will be required to dissect this regulatory mechanism. Moreover, the evidence chain placing LCN2 downstream of the LINC00294/CSTF1 axis, although supported by the reciprocal regulation of LCN2 by LINC00294 and CSTF1 and by the functional phenocopy between LCN2 overexpression and CSTF1 overexpression, lacks formal epistasis tests: neither LCN2 knockdown in LINC00294-overexpressing cells in vitro nor an in vivo LINC00294 + LCN2-silencing rescue group was included, and the subcellular localization of LINC00294, which would underpin the proposed "sponge" model, has not been experimentally determined. In addition, the transduction efficiency of the intratumorally injected lentiviruses was not independently verified in the harvested xenograft tissues, although the robust and reproducible phenotypic, histological, and molecular differences among the three groups indirectly support effective transgene delivery and expression, and the overexpression efficiencies of both constructs were verified in vitro before injection; direct verification of transgene expression in tumor tissues will be performed in future studies. Additionally, the in vivo ferroptosis marker panel is incomplete. FSP1, a key glutathione-independent ferroptosis regulator, was excluded from the in vivo analysis due to poor detection reproducibility in bulk tumor homogenates. Thus, current in vivo ferroptosis regulatory conclusions are drawn primarily from the GPX4-dependent glutathione pathway and ACSL4-mediated lipid metabolism axis, and do not encompass the FSP1-mediated alternative ferroptosis path-

way. Optimized FSP1 detection protocols for solid tumor tissues will be established and validated in follow-up in vivo studies. Furthermore, systemic toxicity was not evaluated by serum biochemistry (liver and kidney function) or histopathological examination of major organs, so the safety conclusions drawn here are limited to body-weight monitoring. The sample size in the clinical correlation analysis was modest, and validation in independent, multicenter cohorts will strengthen translational relevance. Potential batch effects from multi-source datasets may introduce variability; standardized processing pipelines should be applied in follow-up studies.

In summary, this study delineates a lncRNA-governed ferroptosis checkpoint in TNBC. LINC00294 functions as a tumor suppressor by antagonizing CSTF1, which otherwise drives LCN2-associated ferroptosis resistance. This LINC00294/CSTF1-mediated LCN2 regulation represents a candidate therapeutic node: LINC00294 restoration, CSTF1 inhibition, or LCN2 blockade may each converge on reactivating ferroptosis in TNBC. Given the absence of targeted therapies in this subtype, our findings provide a mechanistic rationale for developing lncRNA-centric or ferroptosis-inducing strategies in TNBC.

Acknowledgements

This work was supported by the National Natural Science Foundation of China (General Program, Grant No. 81572582).

Disclosure of conflict of interest

None.

Address correspondence to: Hongjiang Wang, First Affiliated Hospital of Dalian Medical University, No. 193, Lianhe Road, Shahekou District, Dalian 116000, Liaoning, China. E-mail: hjwang@dmu.edu.cn

References

[1] Yan S, Sun X and Wang K. From cold to hot tumors: feasibility of applying therapeutic insights to TNBC. Discov Oncol 2025; 16: 1942.

[2] Qu P, Li X, Liu J, Su X, Han S, Wang Y, Luo Y, Li J, Ma C, Deng S, Hou L, Liang Q and Cheng P. Application of gene editing technology based on targeted delivery materials in TNBC. ACS Omega 2025; 10: 42110-42126.

[3] Fines C, McCarthy H and Buckley N. The search for a TNBC vaccine: the guardian vaccine. Cancer Biol Ther 2025; 26: 2472432.

[4] Lin WD, Chang CH, Pan JK, Lin FC, Chen YC, Chen YJ, Wang PS, Hong WQ, Chen SY, Lin CH, Kuo YL, Chung WP, Cheng HC, Hsiao M, Yang CN and Lu PJ. A novel long non-coding RNA MIR4500HG003 promotes tumor metastasis through miR-483-3p-MMP9 axis in triple-negative breast cancer. Cell Death Dis 2024; 15: 310.

[5] Su Y, Bai Q, Zhang W, Xu B and Hu T. The role of long non-coding RNAs in modulating the immune microenvironment of triple-negative breast cancer: mechanistic insights and therapeutic potential. Biomolecules 2025; 15: 454.

[6] Dalil D, Iranzadeh S, Barouh A, Ghorbanniadelavar Z and Mehrabi MM. The role of long noncoding RNAs in developing paclitaxel-resistant triple negative breast cancer: a systematic review. Cancer Treat Res Commun 2025; 43: 100936.

[7] Hashemi MH, Moaiery H, Nikkhoo B, Zamani F, Mahmoodian S, Soheili M, Soleimani F, Bahramirad Z, KhademErfan M, Ghaderi B, Keyhani ME and Nasseri S. Molecular dynamics of breast cancer subtypes: the role of FAM83H-AS1 long non-coding RNA in breast cancer metastasis. Breast Cancer Res Treat 2025; 210: 645-659.

[8] Zhang Y, Dong X, Guo X, Li C, Fan Y, Liu P, Yuan D, Ma X, Wang J, Zheng J, Li H and Gao P. LncRNA-BC069792 suppresses tumor progression by targeting KCNQ4 in breast cancer. Mol Cancer 2023; 22: 41.

[9] Yuan H, Qin Y, Zeng B, Feng Y, Li Y, Xiang T and Ren G. Long noncoding RNA LINC01089 predicts clinical prognosis and inhibits cell proliferation and invasion through the Wnt/β-catenin signaling pathway in breast cancer. Onco Targets Ther 2019; 12: 4883-4895.

[10] Qi P, Yexie Z, Xue C, Huang G, Zhao Z and Zhang X. LINC00294/miR-620/MKRN2 axis provides biomarkers and negatively regulates malignant progression in colorectal carcinoma. Hum Exp Toxicol 2023; 42: 9603271231167577.

[11] Wang K, Nie Y, Wang S and Chang D. Overexpression of lncRNA LINC00294 induces cell cycle arrest and apoptosis in colorectal cancer by regulating the miR-499a-5p/LARP4B axis. J Biochem Mol Toxicol 2025; 39: e70104.

[12] Zhou X, Lv L, Zhang Z, Wei S and Zheng T. LINC00294 negatively modulates cell proliferation in glioma through a neurofilament medium-mediated pathway via interacting with miR-1278. J Gene Med 2020; 22: e3235.

[13] Qiu J, Zhou S, Cheng W and Luo C. LINC00294 induced by GRP78 promotes cervical cancer

development by promoting cell cycle transition. Oncol Lett 2020; 20: 262.
[14] Zhang R, Yang R, Huang Z, Xu X, Lv S, Guan X, Li H and Wu J. METTL3/YTHDC1-mediated upregulation of LINC00294 promotes hepatocellular carcinoma progression. Heliyon 2023; 9: e22595.
[15] Valashedi MR, Roushandeh AM, Tomita K, Kuwahara Y, Pourmohammadi-Bejarpasi Z, Kozani PS, Sato T and Roudkenar MH. CRISPR/Cas9-mediated knockout of Lcn2 in human breast cancer cell line MDA-MB-231 ameliorates erastin-mediated ferroptosis and increases cisplatin vulnerability. Life Sci 2022; 304: 120704.
[16] Sun G, Wang J, Liu F, Zhao C, Cui S, Wang Z, Liu Z, Zhang Q, Xiang C, Zhang Y, Galons H, Yu P and Teng Y. G-4 inhibits triple negative breast cancer by inducing cell apoptosis and promoting LCN2-dependent ferroptosis. Biochem Pharmacol 2024; 222: 116077.
[17] Yao F, Deng Y, Zhao Y, Mei Y, Zhang Y, Liu X, Martinez C, Su X, Rosato RR, Teng H, Hang Q, Yap S, Chen D, Wang Y, Chen MM, Zhang M, Liang H, Xie D, Chen X, Zhu H, Chang JC, You MJ, Sun Y, Gan B and Ma L. A targetable LIFR-NF-κB-LCN2 axis controls liver tumorigenesis and vulnerability to ferroptosis. Nat Commun 2021; 12: 7333.
[18] Hua Z, White J and Zhou J. Cancer stem cells in TNBC. Semin Cancer Biol 2022; 82: 26-34.
[19] Grosse C, Noack P, Grosse A, Preuss CI, Schwarz HK, Gitter T, Schrenk P, Frauchiger-Heuer H, Papassotiropoulos B, Tausch C, Maccio U, Moch H, Langer R and Varga Z. Prognostic impact of histological subtyping in triple-negative breast cancer. Hum Pathol 2024; 152: 105640.
[20] Wu H, Sun C, Cao W, Teng Q, Ma X, Schiöth HB, Dong R, Zhang Q and Kong B. Blockade of the lncRNA-PART1-PHB2 axis confers resistance to PARP inhibitor and promotes cellular senescence in ovarian cancer. Cancer Lett 2024; 602: 217192.
[21] Liu Y, He J, Chen J, Chen T, Li W, Yang Z and Zeng F. Programmed cell death in triple-negative breast cancer. Cell Mol Biol Lett 2025; 30: 111.
[22] Yun W, Li Y, Huang J and Yuan Y. lncRNA-miRNA/RBP-mRNA network involved in human triple-negative breast cancer: an integrated approach. J Environ Pathol Toxicol Oncol 2025; 44: 75-87.
[23] Huang H, Liang X, Wu W, Yuan T, Chen Z, Wang L, Wu Z, Zhang T, Yang K and Wen K. FOXP3-regulated lncRNA NONHSAT136151 promotes colorectal cancer progression by disrupting QKI interaction with target mRNAs. J Cell Mol Med 2024; 28: e18068.
[24] Zhang N and Wen K. The role of lncRNA binding to RNA-binding proteins to regulate mRNA stability in cancer progression and drug resistance mechanisms (Review). Oncol Rep 2024; 52: 142.
[25] Li S, Lv J, Zhang X, Zhang Q, Li Z, Lu J, Huo X, Guo M, Liu X, Gao R, Gong J, Li C, Li W, Zhang T, Wang J, Chen Z and Du X. ELAVL4 promotes the tumorigenesis of small cell lung cancer by stabilizing LncRNA LYPLAL1-DT and enhancing profilin 2 activation. FASEB J 2023; 37: e23170.
[26] Wu Q, Lu S, Zhang L and Zhao L. LncRNA HOXA-AS2 activates the notch pathway to promote cervical cancer cell proliferation and migration. Reprod Sci 2021; 28: 3000-3009.
[27] Aimaiti M, Maimaitituxun D, Yilihaer X, Kuerban T, Zhu J, Ainiwaer M, Jia Z and Abudourousuli A. Exploring the potential of CSTF1 as a prognostic biomarker in hepatocellular carcinoma and its correlation with immune infiltration. J Hepatocell Carcinoma 2025; 12: 2693-2707.
[28] Keller DT, Weiskirchen R and Schröder-Lange SK. Lipocalin-2 in triple-negative breast cancer: a review of its pathophysiological role in the metastatic cascade. Int J Mol Sci 2025; 26: 10938.
[29] Zhao Y, Tang X, Lei T, Fu D and Zhang H. Lipocalin-2 promotes breast cancer brain metastasis by enhancing tumor invasion and modulating brain microenvironment. Front Oncol 2024; 14: 1448089.
[30] Doll S, Freitas FP, Shah R, Aldrovandi M, da Silva MC, Ingold I, Goya Grocin A, Xavier da Silva TN, Panzilius E, Scheel CH, Mourão A, Buday K, Sato M, Wanninger J, Vignane T, Mohana V, Rehberg M, Flatley A, Schepers A, Kurz A, White D, Sauer M, Sattler M, Tate EW, Schmitz W, Schulze A, O'Donnell V, Proneth B, Popowicz GM, Pratt DA, Angeli JPF and Conrad M. FSP1 is a glutathione-independent ferroptosis suppressor. Nature 2019; 575: 693-698.

Table S1. CSTF1 siRNA sequence

Name	Sequences (5' to 3')
CSTF1 siRNA#1	F: UAGUAGAGAUGGACAGUUATT
	R: UAACUGUCCAUCUCUACUATT
CSTF1 siRNA#2	F: CAUCACAACUUUUGAGAAATT
	R: UUUCUCAAAAGUUGUGAUGTT
CSTF1 siRNA#3	F: GUAGCUAAACUUUGGGAAATT
	R: UUUCCCAAAGUUUAGCUACTT
NC siRNA	F: UUCUCCGAACGUGUCACGUTT
	R: ACGUGACACGUUCGGAGAATT

Table S2. Gene primer sequences for real-time quantitative PCR

Name	Sequences	Amplification length (bp)
LINC00294	F: TAAGGTGGAGGCTGCTCTGTGG	84
	R: ACTCTGAGGCTGAGGCTTCTCTG	
CSTF1	F: ACGGGACGAACACTGGTCAGAT	106
	R: CGGGCAGCAACACATAGTCCTC	
TAGLN	F: TCTGGCTGAAGAATGGCGTGAT	118
	R: TGCTCCATCTGCTTGAAGACCA	
TIMP3	F: GGCTGTGCAACTTCGTGGAGA	119
	R: GCAAGGCAGGTAGTAGCAGGAC	
CCL20	F: GCGAATCAGAAGCAGCAAGCA	122
	R: AGCATTGATGTCACAGCCTTCA	
LCN2	F: GCTACAATGTCACCTCCGTCCT	80
	R: GGGCTGGCAACCTGGAACAA	
GAPDH	F: CAAATTCCATGGCACCGTCA	109
	R: AGCATCGCCCCACTTGATTT	

Table S3. The information of the antibodies

Name	Cat.	Manufacturer	Dilution rate	Application
Rabbit anti-GAPDH	KGC6102-1	KeyGEN BioTECH	1:500	primary antibody
Rabbit anti-ACSL4	bsm-62432R	Bioss	1:1000	primary antibody
Rabbit anti-GPX4	bsm-61552R	Bioss	1:1000	primary antibody
Rabbit anti-FSP1	bsm-55522R	Bioss	1:1000	primary antibody
Mouse anti-LCN2	bsm-41179M	Bioss	1:1000	primary antibody
Rabbit anti-CSTF1	10064-2-AP	Proteintech	1:1000	primary antibody
Goat anti-rabbit IgG(H+L)	KGC6202-0.1	KeyGEN BioTECH	1:2000	secondary antibody
Goat anti-mouse IgG(H+L)	KGC6203-0.1	KeyGEN BioTECH	1:3000	Secondary antibody

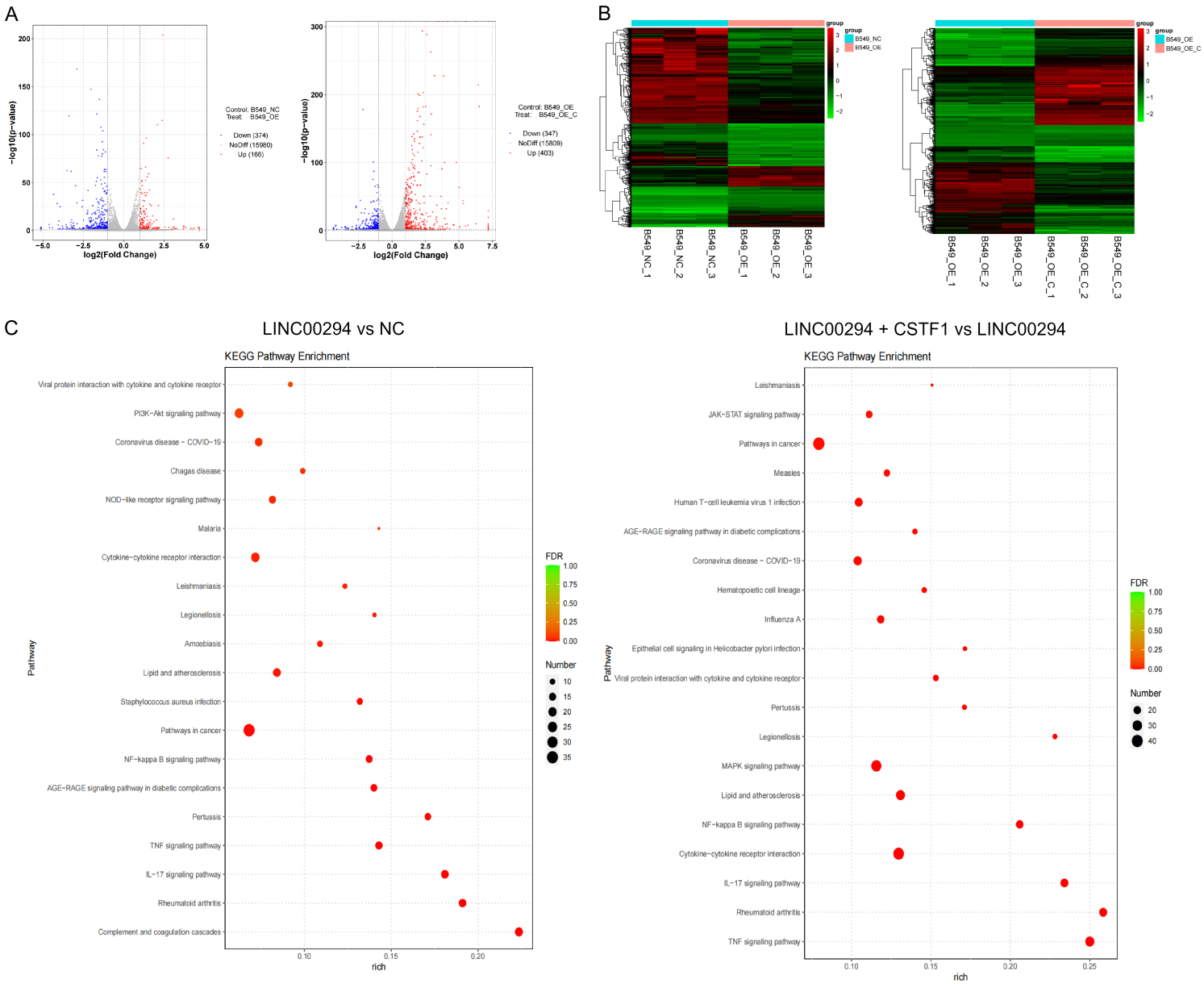

Figure S1. Gene expression profile downstream of the LINC00294/CSTF1 axis. A. Volcano plot. B. Heatmap of differentially expressed genes (DEGs). C. KEGG pathway enrichment analysis.